Nodal chain semimetal in geometrically frustrated systems

Meng Xiao, Xiao-Qi Sun, and Shanhui Fan

Phys. Rev. B **99**, 094206 — Published 25 March 2019

DOI: 10.1103/PhysRevB.99.094206

Nodal Chain Semimetal in Geometrically Frustrated Systems

Meng Xiao,[1] Xiao-Qi Sun,[2] and Shanhui Fan[1,*]

[1]*Department of Electrical Engineering, and Ginzton Laboratory, Stanford University, Stanford, California 94305, USA*

[2]*Department of Physics, Stanford University, California 94305, USA*

Corresponding E-mail:shanhui@stanford.edu

Geometrically frustrated systems and topological semimetals have both attracted much interest and been studied in various systems in recent years. Here we study the interplay between these two systems. We show that a Weyl point can be extended to a chain of degeneracy (a nodal chain) with nonzero charge of Berry flux through geometrical frustration. We propose to realize such a charged nodal chain in an acoustic metamaterial, based on both tight-binding and full-wave numerical simulations. Moreover, we observe a fan-like surface state spectrum, whose dispersion is controlled by the bulk band properties. Our work points to a new class of band degeneracy that carries non-zero Berry flux. The resulting topological metamaterial may be useful for controlling the flow of sound and light.

Subject Areas: Acoustics, Metamaterials, Materials Science.

I. Introduction

Geometrically frustrated systems with a large number of nearly degenerate states are of great interest in the physics of condensed matter [1-6], cold atoms [7-9] and classical waves [10-14]. In these systems, the energy spectrum possesses nondispersive bands and hence interaction becomes important and leads to novel phases of matter.[15-21] On the other hand, topological semimetals, where topologically stable band degeneracies occur, have also attracted widespread attention[22-53]. Such band degeneracies can form a zero-dimensional nodal point[22-39], one-dimensional nodal line[40-49], or two-dimensional nodal surface[43,50-53] in the momentum space. Here we study the interplay between geometrical frustrated lattices and topological semimetals. Within a tight-binding model, we show that geometrical frustration can endow a Weyl point dispersionless directions of the band structure, which then extends the Weyl point to a degenerate nodal line or nodal chain. Such an operation preserves the topological charge and results in a nodal line/chain carrying a nonzero monopole charge. As geometrically frustration is fragile and is usually achieved with fine tuning of the parameters, we propose to realize such a nodal chain with an acoustic metamaterial which offers flexibility in tuning the parameters. We then demonstrate the existence of charged nodal chain numerically with full wave simulations. We also discuss the surface states associated with this system. When the nodal chain is projected onto a single line inside the surface Brillouin zone, the link point of the Fermi-arc on the nodal line can change depending on the boundary condition. When the nodal chain is projected to a crossing inside the surface Brillouin zone, we observe a fan-shaped surface state spectrum instead of the usual drumhead surface states[54,55].

The paper is organized as follows: In Sec. II, we introduce the effective Hamiltonian of a nodal line with nonzero Berry charge and further shows how to construct a charged nodal chain. In Sec. III, we show how to implement this charged nodal chain in a tight-binding model through geometrical frustration. In Sec. IV, we discuss an acoustic metamaterial, which exhibits this charged nodal chain and obtain the Berry charge of the nodal chain through numerically calculating the Chern numbers as a function of k_z. In Sec. V, we continue to discuss the unique surface properties of such a system with a charged nodal chain and then conclude in Sec. VI.

II. Hamiltonian of a nodal line with nonzero Berry charge and construction of a nodal chain

We start with a simple Hamiltonian

$$\hat{H}(\mathbf{k}) = q_x\sigma_x + q_z\sigma_z + f(q_\rho)q_y\sigma_y, \tag{1}$$

where q_x, q_y and q_z are the wavevectors along the *x*, *y*, and *z* directions, respectively, $q_\rho = \sqrt{q_x^2 + q_z^2}$, $f(q_\rho)$ is a real function of q_ρ, and σ_x, σ_y and σ_z are the Pauli matrices. When $f(q_\rho) = 1$, this Hamiltonian gives the Weyl Hamiltonian with topological charge $+1$; when $f(q_\rho) = 0$, it becomes

$$\hat{H}(\mathbf{k}) = q_x\sigma_x + q_z\sigma_z. \tag{2}$$

This Hamiltonian describes a nodal line along the *y*-direction. The system in this case exhibits $\mathcal{PT}$ symmetry (note the absence of σ_y term in Eq. (2), and here $\mathcal{P}$ and $\mathcal{T}$ represent inversion and time reversal operators, respectively.), hence the Berry curvature vanishes at every ***k***-point and the nodal line is not charged. To create a charged nodal line, we instead consider the case $f(q_\rho) = 0$ only at $q_\rho = 0$, and as a special case $f(q_\rho) = q_\rho$, i.e.,

$$\hat{H}(\mathbf{k}) = q_x\sigma_x + q_z\sigma_z + q_\rho q_y\sigma_y. \tag{3}$$

This Hamiltonian possesses a nodal line along the *y*-direction as the bands are degenerate at $q_\rho = 0$ and exhibits linear dispersion when away from this nodal line. The Berry curvature for the Hamiltonian in Eq. (3) has the form:

$$\mathbf{B}_\pm = \mp\frac{1 + 2q_z^2 - 2q_z\sqrt{1+q_z^2}}{q_\rho\left(2 + 2q_z^2 - 2q_z\sqrt{1+q_z^2}\right)}\hat{q}_\rho, \tag{4}$$

where $\hat{q}_\rho$ represents the radial direction, and the subscripts "+" and "–" correspond to the upper and lower bands, respectively. In Fig. 1(a), we show the Berry flux density distribution (arrows) around this nodal line (red line) and the quantized charge carried by the nodal line is +1, which is obtained by integrating the total Berry flux through a cylindrical surface enclosing this nodal line.

Comparing Eqs. (2) and (3), we see the Hamiltonian in Eq. (2), which only supports a non-charged nodal line, has no σ_y term for *every* q_x and q_z. In contrast, the coefficient before σ_y of the Hamiltonian in Eq. (3), which supports a charged nodal line, vanishes *only* at $q_\rho = 0$. Meanwhile, the charged nodal line in Eq. (3) exhibits non-dispersive band along the y direction at $q_\rho = 0$ which is reminiscent of the geometric frustration that can be utilized to create non-dispersive band along special directions. [1-14] Therefore, it is natural to consider the use of geometric frustration to realize a charged nodal line.

For any nodal line, the charge of Berry flux is quantized due to gauge invariance. In a periodic system, nodal lines can extend across the Brillouin zone with ends meeting at the zone boundary, or form closed loops inside the Brillouin zone and these loops can be either isolated [40-42], linked [44-47] or connected into a chain [47-49]. For example, we consider the special case in which two nodal lines intersect with each other and both extend across the entire Brillouin zone. A schematic picture is shown in Fig. 1(b), where two nodal lines (represented by the red cylinders) are assumed to be on the $k_z = \pi$ plane one at $k_x = 0$ and the other at $k_y = 0$. Here $\left(k_x, k_y, k_z\right)$ denotes the position in the reciprocal space. Considering the fact that the Brillouin zone is periodic, this configuration in Fig. 1(b) is topologically equivalent to the two nodal rings chained together as shown in Fig. 1(c). For the discussion below, we also call the connection of two nodal rings as shown in Fig. 1(c) nodal chain for simplicity. Indeed, our case can be regarded as a simplified version (only two rings chained together) of the nodal chains discussed in Refs. [47-49] wherein there are more nodal rings chained together. Here the positions of nodal lines are not limited to be on the $k_z = \pi$ plane. As we will show later, a nodal chain of this form with non-zero charge can exist in geometrically frustrated lattices.

III. Tight-binding model with flat nodal chain

To achieve a charged nodal line using the concept of geometric frustration, we consider a tight-binding model as shown in Fig. 2(a). This model has no spin degree of freedom. Each unit cell consists of four inequivalent sublattices represented by spheres with different colors and all sublattices share the same onsite energy. This structure consists of layers equally spaced along the z direction, with each sublattice

on each layer forming a square lattice with a lattice constant a. The second, third and fourth layers are translated by $(0, a/2)$, $(a/2, a/2)$ and $(a/2, 0)$ in the *xy*-plane respectively, with respect to the first layer. Coupling occurs only between layers. There are two types of couplings denoted as black and yellow bonds in Fig. 2(a), respectively. The black bond occurs between adjacent layers with strength t_0. The yellow bond occurs between next adjacent layers. The hopping strength of such bonds varies depending on the projected locations in the *x*-*y* plane as shown in Fig. 2(b), and has strength of either $t_1 = (1+\delta)t_c$, $t_2 = (1-\delta)t_c$ with δ being a small number. Our system is assumed to preserve time reversal symmetry, and hence the hopping constants are all real. The explicit form of this Hamiltonian can be found in Appendix A. Figure 2(c) shows the reciprocal space of this tight-binding model and some high symmetric points are also labeled.

Figure 3(a) shows the band structure of this tight-binding model along some high symmetric directions with $t_0 = -2\sqrt{2}$, $t_c = -1$ and $\delta = 0.1$. There are in total four bands and we label them respectively as band 1 (black), 2 (red), 3 (blue), and 4 (magenta) from low energy to high energy. There are a few band degeneracy points between these bands, which are either Weyl points or degeneracy points without charge. The degeneracy point between band 1 and band 2 at Z does not exhibit any topological charge. The degeneracy point at S between band 2 and band 3 is a charge -2 Weyl point, and the degeneracy on ΓZ at $k_z h = 0.34\pi$ is a charge +1 Weyl point. Due to time reversal symmetry, there is another Weyl point with the same charge at $k_z h = -0.34\pi$ with charge $+1$. The degeneracy point at Γ between band 3 and band 4 is another Weyl point with charge $+2$. There is no other band degeneracy point. Meanwhile, the values of t_0 and t_c are chosen to satisfy the condition $t_0 = 2\sqrt{2}t_c$ such that the charge +2 Weyl point at Γ and the charge -2 Weyl point at Z between band 3 and band 4 are at the same energy. (See detailed discussion in Appendix A)

In Fig. 3(b), we show the band structure with $\delta = 0$ while keep the other parameters unchanged. The band structures are quite similar like each other except one distinct difference: Band 1 (3) and band 2 (4) are degenerate along the ZU and ZT directions. Band 2 and band 3 are degenerate along the SX and SY directions. These nodal lines are also highlighted in Fig. 2(c) in red. Hence this tight-binding model

possesses three nodal chains. In contrast with the symmetry-protected nodal lines as discussed in Ref. [40-49] which all exhibit dispersion along the line. Here we note that the nodal chains in our system are dispersionless which is in sharp contrast with the nodal lines protected by spatial symmetries. This is reminiscent of the geometrically frustrated lattices where perfect flat bands are also found. Geometrically frustrated systems with a large degeneracy of states has been explored in model systems such as Dice lattice [15], Lieb' s lattice [17], Kagome lattice [18-20] and Tasaki' s decorated square lattice [21]. Recently, the mechanism and associated phenomena are also intensely investigated in the context of condensed matter physics [1-6], cold atoms [7-9], and photonic crystals [10-14]. The essential idea is to design a lattice whose inter unit cell couplings vanish under certain circumstance. In our system, the inter unit cell coupling is controlled solely by the yellow bonds in Fig. 2(b), and has the form of (see Appendix A for more details)

$$\left|\hat{H}_{13}\right| = \left|\hat{H}_{24}\right| = 4\left|t_c\right| \sqrt{\cos^2\left(\frac{k_x}{2}\right)\cos^2\left(\frac{k_y}{2}\right)\cos^2\left(\frac{k_z}{2}\right) + \sin^2\left(\frac{k_x}{2}\right)\sin^2\left(\frac{k_y}{2}\right)\sin^2\left(\frac{k_z}{2}\right)}, \quad (5)$$

where $\hat{H}_{13}$ and $\hat{H}_{24}$ refer to the coupling between sublattices 1 and 3, and between sublattices 2 and 4, respectively. At $k_i = 0$ and $k_j = \pi$, where $i, j \in \{x, y, z\}$ and $i \neq j$, both $\left|\hat{H}_{13}\right|$ and $\left|\hat{H}_{24}\right|$ vanish. Along these special directions, the inter unit cell couplings in the *x*-*y* plane vanish in this tight-binding model. Hence one can conclude that all the bands become nondispersive along the highlighted directions in Fig. 2(c), i.e., $k_z = \pi$ and $k_x = 0$ or $k_y = 0$, and $k_z = 0$ and $k_x = \pi$ or $k_y = \pi$. These highlighted directions are the only directions along which the bands are dispersionless as ensured by the geometric frustration. Under the condition that the coupling introduced by the yellow bonds vanishes, the remaining system exhibits four-fold screw symmetry $\tilde{C}_4$ along the *z* direction. $\tilde{C}_4$ symmetry requires that band 2 and band 3 are degenerate at Γ, band 1 and band 2 are degenerate at Z, and band 3 and band 4 are also degenerate at *Z*. Combining with the fact that the bands are dispersionless along the highlighted directions in Fig. 2(c), we can now conclude that the system exhibits perfectly-flat nodal lines along those highlighted directions. Note here the nodal lines are not necessarily dispersionless even in geometrically frustrated systems; they are flat only along the special directions where geometric frustration condition is satisfied.

As another evidence of geometric frustration, we show the amplitude of the eigenstates on the flat nodal line at $k_x = \pi$ or $k_y = \pi$ in the inset of Fig. 3(b). There are two degenerate states on this nodal line. One has nonzero opposite amplitude only on sublattices 1 and 3, and the other has nonzero opposite amplitude only on sublattices 2 and 4. We note that all the eigenstates on these two flat bands are the same except for a global phase factor. The amplitude distribution is consistent with those of the flat bands in other geometrically frustrated systems [11-13]. Geometric frustration in Fig. 3(b) extends the degeneracies at *S* and *Z* in Fig. 3(a) along the *x*-axis and *y*-axis and form dispersionless nodal chain. As this process does not change the topological charge, whether the nodal chain formed carries a topological charge or not only depends on the topological charge of the original degeneracy. Combined with the charge analysis before, we can conclude that the nodal chain between band 1 and band 2 are not charged, while the other two nodal chains carry a topological charge -2. The consequence of geometric frustration can also be seen from the Berry flux density distribution near the charged objects as shown in Figs. 3(c) and 3(d). Here we choose band 4 as an example and fix $k_z h = 0.999\pi$. When $\delta = 0.1$, the Berry flux concentrates around $k_x = k_y = 0$ as all the Berry flux originates from the Weyl point at Z point. While for $\delta = 0$, the Berry flux spreads out around the nodal lines along $k_x = 0$ and $k_y = 0$ directions due to the geometric frustration.

IV. Acoustic metamaterial realization

The geometrically frustrated lattice proposed above can be realized with acoustic metamaterials. The side view and top view of a unit cell of such an acoustic metamaterial is shown in Figs. 4(a) and 4(b), respectively. Here blue and yellow represent the surfaces where hard boundary and periodic boundary conditions are applied, respectively. The basic idea for this design is to replace the lattice sites with resonance cavities that are formed within the hard boundaries. Between the cavities, tubes are added in to connect sites and introduce hopping. The hopping strength is proportional to the cross section of these connecting tubes. The merit of this metamaterial is to allow one to specifically design the desired hopping configurations, and this acoustic metamaterial platform has been previously used experimentally to demonstrate various topological concepts[56-58]. The band dispersion along several high symmetric directions is shown in Fig. 4(c). The band formed from the the lowest order mode of the resonance cavities is linear in the low frequency limit. Except for that, other features of the band

structures in Figs. 3(b) and 4(c) are quite similar. In particular, we have flat nodal chains as predicted by the tight-binding model in Fig. 2.

Berry charge of nodal chain

Now we proceed to show that some of these flat nodal chains possess nonzero charge of Berry flux with full wave simulations. The analysis of the Berry charges of the tight-binding model can be found in Appendix A. In such a system with time reversal symmetry, the charge of Berry flux can only be carried by band degeneracies, at either points, lines or surfaces. Besides the nodal line degeneracies discussed before, there are point band degeneracy at Γ between band 3 and band 4, and on ΓZ at $k_z = 0.18\pi / h$ between band 2 and band 3, which together complete the set of band degeneracies in this system. This conclusion is consistent with the tight-binding model, which provides a good description of the acoustic metamaterial.

To obtain the charge of Berry flux for these band degenerate points, we calculate the Chern number for two-dimensional bands with fixed k_z as shown in Fig. 5, where Figs. 5(a-d) show the Chern numbers of bands 1-4, respectively. (More details can be found in Appendix B.) In Fig. 5(a), we see that the Chern number is zero for all the k_z. Hence we can conclude that the Berry charge of the nodal chain between band 1 and band 2 is zero, which is marked in gray on the left panel of Fig. 5(a). In Fig. 5(b), the Chern number increases by 1 at $k_z = \pm 0.18\pi / h$, and hence the band structure possesses two charge +1 Weyl points at $k_z = \pm 0.18\pi / h$ on ΓZ as represented by the yellow sphere in Fig. 5(b). Meanwhile, the Chern number decreases by 2 across the nodal chain at $k_z = 0$, which then indicates that the Berry charge of the nodal chain between band 2 and band 3 is -2 as marked by the cyan lines on the left panel of Fig. 5(b). In Fig. 5(c), the Chern number is -1 for $0.18 < k_z h / \pi < 1$, and hence the nodal chain between band 3 and band 4 is -2 as highlighted by cyan line on the left panel of Fig. 5(c). Meanwhile, the Chern number increases by 4 at $k_z = 0$. This comes from two parts: the nodal chain between band 2 and band 3, and the Weyl point at Γ. Hence the charge of this Weyl point is $+2$ and we use a red sphere on the left panel of Fig. 5(c) to denote it. According to the analysis before, we know the Berry charge of the nodal chain and Weyl point as shown on the left panel of Fig. 5(d), which are respectively -2 and $+2$.

Considering the fact that the Chern number is opposite for opposite k_z, we know the Chern number of band 4 should be +1 for $k_z > 0$ and -1 for $k_z < 0$. This above conclusion is consistent with the results from numerical simulations as shown on the right panel of Fig. 5(d).

V. Fermi-arcs and fan-like surface states

The nonzero Chern numbers associated with the charged nodal chains indicate the existence of chiral edge states. In Fig. 6(a), we show the projected band structure at $k_z h = 0.5\pi$ using a ribbon structure as shown in Fig. 6(b). This ribbon is periodic along the *y* and *z* directions, and finite along the *x* direction. The number of unit cell along the *x* direction is chosen to be large enough such that the dispersions of the edge states converge as we further increase the number of unit cell. The gray area in Fig. 6(a) shows the projection of bulk bands and the gray curves represent the dispersion of the trivial edge states. There are two chiral edge states in the band gap between band 3 and band 4, where the red and cyan curves represent the edge states localized on the right and left edges of the ribbon, respectively. The existence of these chiral edge states is consistent with the Chern numbers calculated in Fig. 5. In Fig. 6(b), we also show the absolute value of the eigenpressure field of the edge state at $k_y a = 0.1\pi$ and 200.9 Hz, where red and blue correspond to maximum value and zero, respectively. The field is well localized on the boundary.

The equal frequency cut of these chiral edge states defines the "Fermi arcs". The Fermi arcs in this system connect the projections of the Weyl points and the charge nodal chains. Comparing the band structures from tight-binding model in Fig. 3(b) and full wave simulation in Fig. 4, we see that the tight-binding model can describe the metamaterial quite well. And hence we use the tight-binding model to reduce the simulation workload for the following surface state calculations. From the band structure, we can see that there are complete bandgaps between band 1 and band 2, and between band 3 and band 4 for any k_z except $k_z h \neq \pm\pi$. From the Chern number calculation, we can see that the gap between band 1 and band 2 is topologically trivial, while the bandgap between band 3 and band 4 is topologically nontrivial. Hence for the discussion below, we will focus on the bandgap between band 3 and band 4.

As discussed before (and can also be seen in Appendix A), one can tune the hopping constant t_0 and t_c to achieve the condition $t_0 = 2\sqrt{2}t_c$ and then the nodal chain and Weyl point between band 3 and band 4 are at the same energy. After projected onto the $k_y - k_z$ surface Brillouin zone, the nodal chains become straight lines at $k_z h = \pm\pi$ as highlighted by cyan in Fig. 6(c). The charge $+2$ Weyl point is projected to a point [denoted by the red point in Fig. 6(c)] at $k_y = k_z = 0$. According to the surface bulk correspondence, there should be two Fermi-arcs connecting the charge +2 Weyl point and charge -2 nodal chain. Different from the Fermi-arcs between Weyl points, here the Fermi-arc connects a Weyl point and a nodal chain, and the link point on the projection of nodal chain actually depends on the boundary conditions. We consider a semi-infinite system, which is truncated at the $-x$ side with different truncations as shown with the two insets in Fig. 6(c). The Fermi-arcs at the energy of the Weyl point (also the energy of the nodal chain) with two truncations are shown in Fig. 6(c), where black and magenta represents the cases when sublattice 1 (2) is the outmost sublattice (see the inset on the lower right) and sublattice 3(4) is the outmost sublattice (see the inset on the upper left), respectively. Indeed, as we change the boundary condition, the link point slides on the cyan line.

Besides changing of the link point of the Fermi-arc on the projection of nodal chain, this system also exhibits interesting surface states behaviors when truncated along the z direction. In this case, the nodal chain is projected onto two lines crossing at Γ and the charge +2 Weyl point is located at Γ, inside the $k_x - k_y$ surface Brillouin zone. In the inset of Fig. 7(b), we show the nodal lines (cyan lines) as well as the Weyl point (red sphere). Figure 7(a) shows the surface states in the bandgap between band 3 and band 4 for a semi-infinite system, which is truncated on the $+z$ direction and with sublattice 4 on the outmost. Here for simplicity, we only show the spectrum of the surface states. It is quite interesting that, instead of the drumhead surface state [54,55], here we observe a "fan-like" surface state spectrum. To understand this "fan-like" spectrum of the surface state, we turn to the Zak phase distribution. Here we consider the Zak phase of a one-dimensional band with fixed k_x and k_y, and the Zak phase gives the center of Wannier function of that one-dimensional band [59,60]. Now we consider the Zak phase θ (see definition given by the inset in Fig. 7(b)) of band 4 along a circle around Γ as a function of the polar angle φ. The corresponding result is shown in Fig. 7(b) with the black curve, where we set

$a\sqrt{k_x^2+k_y^2}=0.1\pi$. The Zak phase almost falls inside the region $(-0.5\pi, 0.5\pi)$. The +2 Weyl point introduces a winding number of 2 of the Zak phase as a function of φ, and each time when crossing the nodal line, the Zak phase jumps a value of around π. Hence the presence of the +2 Weyl point together with the nodal lines give rise to the winding of Zak phase in Fig. 7(b). Figure 7(c) shows the Zak phase (color code) of band 4 in the $k_x - k_y$ surface Brillouin zone. The equal Zak phase contour demonstrates the feature of a fan structure. As the Zak phase represents the position of Wannier center, the dispersion of surface state should also be manifested by the distribution of Zak phase. Different truncations of boundary also affect the dispersion of surface state. When the boundary coincides with the center of Wannier function, there will be a Tamm-like states at the "zero energy" (Here the energy of the nodal lines and Weyl point). Otherwise, there will be no surface states at the "zero energy". As an illustration, Fig. 7(d) shows a fan-like surface arc at the energy of the nodal chain where we truncate the semi-infinite system with sublattice 3 on the outmost. Here we plot the density of state of the unit cell on the surface (surface local density of states) [61,62]. It can be seen that the Fermi-arc follows the equal Zak phase contour and shapes into a fan-like structure.

VI. Discussion and conclusion

Our work demonstrate that nodal chains can possess a nonzero Berry charge, which is a new class of band degeneracy that carries the charge of Berry flux. This work hence provides new possibilities of engineering the topological charge and Berry flux distributions in the momentum space. Meanwhile, as the link point of surface arc states on the charged nodal line can shift, the propagation direction of surface waves can be easily manipulated by changing the boundary condition. When the flat band introduced by the geometric frustration lattice is broken, the nodal line degeneracy is lifted and the nodal chain breaks into a nodal line and/or Weyl points. However, the degeneracy between two bands is still protected by the nonzero charge of Berry flux of the nodal chain. The acoustic metamaterial studied in our work allows us to specifically design the desired hopping configurations, which hence provides a promising platform for studying geometrically frustrated lattice and associated various interesting phenomena [2,16,63]. The large density of states introduced by geometrical frustration is useful under circumstance such as Purcell effect[64]. Similar effects should also be observable for electromagnetic waves.

Acknowledgments

This work is supported by a Vannevar Bush Faculty Fellowship from the U. S. Department of Defense (Grant No. N00014-17-1-3030), and by the U. S. National Science Foundation (Grant No. CBET-1641069).

Appendix A: Tight binding model

The Hamiltonian of the tight binding model in Fig. 2(a) is:

$$\hat{H} = \left(\hat{H}_{ij}\right), \text{ where } i, j \in \{1,2,3,4\}, \tag{A1}$$

where

$$\hat{H}_{12} = t_0 \exp\left[i\left(k_y a/2 + k_z h/4\right)\right],\ \hat{H}_{23} = t_0 \exp\left[i\left(k_x a/2 + k_z h/4\right)\right]$$

$$\hat{H}_{34} = t_0 \exp\left[i\left(-k_y a/2 + k_z h/4\right)\right],\ \hat{H}_{14} = t_0 \exp\left[i\left(k_x a/2 - k_z h/4\right)\right]$$

$$\hat{H}_{13} = 4t_c\left\{\cos\left(\frac{k_x a}{2}\right)\left[\cos\left(\frac{k_y a}{2}\right) + i\delta\sin\left(\frac{k_y a}{2}\right)\right]\cos\left(\frac{k_z h}{2}\right) + \sin\left(\frac{k_x a}{2}\right)\left[i\sin\left(\frac{k_y a}{2}\right) + \delta\cos\left(\frac{k_y a}{2}\right)\right]\sin\left(\frac{k_z h}{2}\right)\right\}$$

$$\hat{H}_{24} = 4t_c\left\{\left[\cos\left(\frac{k_x a}{2}\right) + i\delta\sin\left(\frac{k_x a}{2}\right)\right]\cos\left(\frac{k_y a}{2}\right)\cos\left(\frac{k_z h}{2}\right) - \left[i\sin\left(\frac{k_x a}{2}\right) + \delta\cos\left(\frac{k_x a}{2}\right)\right]\sin\left(\frac{k_y a}{2}\right)\sin\left(\frac{k_z h}{2}\right)\right\}$$

$$\hat{H}_{ii} = 0,\ \hat{H}_{ij} = \hat{H}_{ji}^{*}$$

, (A2)

We can obtain the eigenvalues at some special points. At Γ, the eigenvalues are $-4t_c$, $-4t_c$, and $4t_c \pm 2t_0$. At S, the eigenvalues are $\pm 2t_0$ and 0 with doubly degeneracy. At Z, the eigenvalues are $\pm\sqrt{2}t_0$ and both are doubly degenerate. And the eigenvalues at the above special points are independent of δ. Hence if we set $t_0 = 2\sqrt{2}t_c$, the doubly degenerate point at Γ and Z between band 3 and band 4 are at the same energy.

In the right panel Fig. 8, we show the Chern number as a function of k_z using the tight binding model, where we set $t_0 = -2\sqrt{2}$ and $t_c = -1$. The Chern numbers are numerically calculated with the discretized method discussed in Ref. [65]. We note that here the Chern number is independent of δ when δ is small enough such that there is no additional band crossing point. The topological charges in this system are carried by the band degeneracy points or lines. And hence we can obtain the topological charge distribution as shown in the right and middle panels of Fig. 8. Geometric frustration extends the band degeneracy points in the left panel to nodal chains in the middle panel. Whether the nodal chain is charged or not depends on whether the original degeneracy point is charged or not. The above results are consistent with the one in Fig. 6 computed with fullwave simulations with only the shift of the Weyl point between band 2 and band 3. Hence the charge of Weyl points and nodal chains from the analysis in the main text and are the same as that in the acoustic metamaterial.

Appendix B: Numerical calculation of Chern number

In this section, we give more details of the Chern number calculation in Fig. 5. As discussed in the main text, there are only band degeneracies with k_z at $k_z h = 0$, $\pm 0.18\pi$ and $\pm\pi$. Meanwhile, as the Chern number changes only when passing those band degeneracies, we just need to calculate Chern number for any k_z s between these values, and there we choose $k_z h = 0.5\pi$ and $k_z h = 0.1\pi$. These k_z values are away from the degneracies and thus the numerical calcualtion converges fast. The Chern number for negative k_z can be obtained through $C(k_z) = -C(-k_z)$ since the system exhibits time-reversal symmetry.

The Chern number is obtained through the winding number of the Zak phase [66]. In Fig. 9, we show the Zak phases (denoted by θ) of each band as functions of k_x at $k_z h = 0.5\pi$ [Fig. 9(a)] and $k_z h = 0.1\pi$ [Fig. 9(b)], where black, red, blue and magenta represent the Zak phases of band 1, 2, 3 and 4, respectively. Here the definition of θ is given by

$$\theta = \int_{-\pi}^{\pi} dk_y i \left\langle u\left(k_x, k_y, k_z\right) \right| \frac{\partial}{\partial k_y} \left| u\left(k_x, k_y, k_z\right) \right\rangle, \tag{B1}$$

where $u\left(k_x, k_y, k_z\right)$ represents the periodic part of the pressure field. The winding of the Zak phase as a function of k_x gives the Chern number of that band at fixed k_z [66]. Accordingly, the Chern number at $k_z h = 0.5\pi$ of bands 1, 2, 3 and 4 are 0, 0, -1 and +1, respectively; and the Chern number at $k_z h = 0.1\pi$ of bands 1, 2, 3 and 4 are 0, +1, -2 and +1, respectively. Considering the fact that the Chern number can only change at band degeneracies, we now have the Chern numbers as functions of k_z of each band as shown on the right column of Fig. 5,

References:

[1] Y. Zhou, K. Kanoda, and T.-K. Ng, Rev. Mod. Phys. **89**, 025003 (2017).
[2] L. Balents, Nature **464**, 199 (2010).
[3] P. A. Lee, Science **321**, 1306 (2008).
[4] H. T. Diep, *Frustrated spin systems* (World Scientific, 2004).
[5] C. Lacroix, P. Mendels, and F. Mila, *Introduction to Frustrated Magnetism: Materials, Experiments, Theory* (Springer Berlin Heidelberg, 2011).
[6] R. Drost, T. Ojanen, A. Harju, and P. Liljeroth, Nat. Phys. **13**, 668 (2017).
[7] G.-B. Jo, J. Guzman, C. K. Thomas, P. Hosur, A. Vishwanath, and D. M. Stamper-Kurn, Phys. Rev. Lett. **108**, 045305 (2012).
[8] R. Shen, L. B. Shao, B. Wang, and D. Y. Xing, Phys. Rev. B **81**, 041410 (2010).
[9] S. Taie, H. Ozawa, T. Ichinose, T. Nishio, S. Nakajima, and Y. Takahashi, Sci. Adv. **1**, e1500854 (2015).
[10] T. Hiroyuki, T. Tetsuya, and Y. Katsumi, J. Phys. Condens. Matter **16**, 6317 (2004).
[11] Y. Nakata, T. Okada, T. Nakanishi, and M. Kitano, Phys. Rev. B **85**, 205128 (2012).
[12] M. Nixon, E. Ronen, A. A. Friesem, and N. Davidson, Phys. Rev. Lett. **110**, 184102 (2013).
[13] R. A. Vicencio, C. Cantillano, L. Morales-Inostroza, B. Real, C. Mejía-Cortés, S. Weimann, A. Szameit, and M. I. Molina, Phys. Rev. Lett. **114**, 245503 (2015).
[14] S. A. Schulz, J. Upham, L. O'Faolain, and R. W. Boyd, Opt. Lett. **42**, 3243 (2017).
[15] B. Sutherland, Phys. Rev. B **34**, 5208 (1986).
[16] D. Leykam, A. Andreanov, and S. Flach, Adv. Phys.: X **3**, 1473052 (2018).
[17] E. H. Lieb, Phys. Rev. Lett. **62**, 1927 (1989).
[18] A. Mielke, J. Phys. A **24**, L73 (1991).
[19] A. Mielke, J. Phys. A **24**, 3311 (1991).
[20] V. Elser, Phys. Rev. Lett. **62**, 2405 (1989).
[21] H. Tasaki, Phys. Rev. Lett. **69**, 1608 (1992).
[22] X. Wan, A. M. Turner, A. Vishwanath, and S. Y. Savrasov, Phys. Rev. B **83**, 205101 (2011).
[23] B. A. Bernevig, Nat. Phys. **11**, 698 (2015).
[24] S.-Y. Xu, I. Belopolski, N. Alidoust, M. Neupane, G. Bian, C. Zhang, R. Sankar, G. Chang, Z. Yuan, C.-C. Lee, S.-M. Huang, H. Zheng, J. Ma, D. S. Sanchez, B. Wang, A. Bansil, F. Chou, P. P. Shibayev, H. Lin, S. Jia and M. Z. Hasan, Science **349**, 613 (2015).
[25] B. Q. Lv, H. M. Weng, B. B. Fu, X. P. Wang, H. Miao, J. Ma, P. Richard, X. C. Huang, L. X. Zhao, G. F. Chen, Z. Fang, X. Dai, T. Qian and H. Ding, Phys. Rev. X **5**, 031013 (2015).
[26] A. A. Soluyanov, D. Gresch, Z. Wang, Q. Wu, M. Troyer, X. Dai, and B. A. Bernevig, Nature **527**, 495 (2015).
[27] L. Lu, L. Fu, J. D. Joannopoulos, and M. Soljačić, Nat. Photonics **7**, 294 (2013).
[28] L. Lu, Z. Wang, D. Ye, L. Ran, L. Fu, J. D. Joannopoulos, and M. Soljačić, Science **349**, 622 (2015).
[29] W.-J. Chen, M. Xiao, and C. T. Chan, Nat. Commun. **7**, 13038 (2016).
[30] M. Xiao, W.-J. Chen, W.-Y. He, and C. T. Chan, Nat. Phys. **11**, 920 (2015).
[31] M. Xiao, Q. Lin, and S. Fan, Phys. Rev. Lett. **117**, 057401 (2016).
[32] W. Gao, B. Yang, M. Lawrence, F. Fang, B. Béri, and S. Zhang, Nat. Commun. **7**, 12435 (2016).
[33] C. Fang, L. Lu, J. Liu, and L. Fu, Nat. Phys. **12**, 936 (2016).
[34] S. Young, S. Zaheer, J. Teo, C. Kane, E. Mele, and A. Rappe, Phys. Rev. Lett. **108**, 140405 (2012).

[35] Z. K. Liu, B. Zhou, Y. Zhang, Z. J. Wang, H. M. Weng, D. Prabhakaran, S.-K. Mo, Z. X. Shen, Z. Fang, X. Dai, Z. Hussain and Y. L. Chen, Science **343**, 864 (2014).
[36] Z. Wang, Y. Sun, X.-Q. Chen, C. Franchini, G. Xu, H. Weng, X. Dai, and Z. Fang, Phys. Rev. B **85**, 195320 (2012).
[37] J. Noh, S. Huang, D. Leykam, Y. D. Chong, K. P. Chen, and M. C. Rechtsman, Nat. Phys. **13**, 611 (2017).
[38] A. B. Khanikaev, Nat. Phys. **13**, 532 (2017).
[39] F. Li, X. Huang, J. Lu, J. Ma, and Z. Liu, Nat. Phys. **14**, 30 (2018).
[40] C. Fang, Y. Chen, H.-Y. Kee, and L. Fu, Phys. Rev. B **92**, 081201 (2015).
[41] C. Fang, H. Weng, X. Dai, and Z. Fang, Chin. Phys. B **25**, 117106 (2016).
[42] A. A. Burkov, M. D. Hook, and L. Balents, Phys. Rev. B **84**, 235126 (2011).
[43] T. Bzdušek and M. Sigrist, Phys. Rev. B **96**, 155105 (2017).
[44] Z. Yan, R. Bi, H. Shen, L. Lu, S.-C. Zhang, and Z. Wang, Phys. Rev. B **96**, 041103 (2017).
[45] W. Chen, H.-Z. Lu, and J.-M. Hou, Phys. Rev. B **96**, 041102 (2017).
[46] X.-Q. Sun, B. Lian, and S.-C. Zhang, Phys. Rev. Lett. **119**, 147001 (2017).
[47] G. Chang, S.-Y. Xu, X. Zhou, S.-M. Huang, B. Singh, B. Wang, I. Belopolski, J. Yin, S. Zhang, A. Bansil, H. Lin and M. Z. Hasan, Phys. Rev. Lett. **119**, 156401 (2017).
[48] Q. Yan, R. Liu, Z. Yan, B. Liu, H. Chen, Z. Wang, and L. Lu, Nat. Phys. **14**, 461 (2018).
[49] T. Bzdušek, Q. Wu, A. Rüegg, M. Sigrist, and A. A. Soluyanov, Nature **538**, 75 (2016).
[50] C. Zhong, Y. Chen, Y. Xie, S. A. Yang, M. L. Cohen, and S. B. Zhang, Nanoscale **8**, 7232 (2016).
[51] Q.-F. Liang, J. Zhou, R. Yu, Z. Wang, and H. Weng, Phys. Rev. B **93**, 085427 (2016).
[52] M. Xiao, and S. Fan, Topologically Charged nodal surface, arXiv:1709.02363 (2017).
[53] G. Chang, B. J. Wieder, F. Schindler, D. S. Sanchez, I. Belopolski, S.-M. Huang, B. Singh, D. Wu, T.-R. Chang, T. Neupert, S.-Y. Xu, H. Lin and M. Z. Hasan, Nat. Mater. **17**, 978 (2018).
[54] Y. H. Chan, C.-K. Chiu, M. Y. Chou, and A. P. Schnyder, Phys. Rev. B **93**, 205132 (2016).
[55] G. Bian, T.-R. Chang, H. Zheng, S. Velury, S.-Y. Xu, T. Neupert, C.-K. Chiu, S.-M. Huang, D. S. Sanchez, I. Belopolski, N. Alidoust, P.-J. Chen, G. Chang, A. Bansil, H.-T. Jeng, H. Lin and M. Z. Hasan, Phys. Rev. B **93**, 121113 (2016).
[56] M. Xiao, G. Ma, Z. Yang, P. Sheng, Z. Q. Zhang, and C. T. Chan, Nat. Phys. **11**, 240 (2015).
[57] Z. Yang and B. Zhang, Phys. Rev. Lett. **117**, 224301 (2016).
[58] Y. X. Xiao, G. Ma, Z. Q. Zhang, and C. T. Chan, Phys. Rev. Lett. **118**, 166803 (2017).
[59] J. Zak, Phys. Rev. Lett. **62**, 2747 (1989).
[60] R. D. King-Smith and D. Vanderbilt, Phys. Rev. B **47**, 1651 (1993).
[61] M. P. L. Sancho, J. M. L. Sancho, J. M. L. Sancho, and J. Rubio, J. Phys. F **15**, 851 (1985).
[62] M. P. L. Sancho, J. M. L. Sancho, and J. Rubio, J. Phys. F **14**, 1205 (1984).
[63] A. P. Ramirez, Annu. Rev. Mater. Sci. **24**, 453 (1994).
[64] M. Landi, J. Zhao, W. E. Prather, Y. Wu, and L. Zhang, Phys. Rev. Lett. **120**, 114301 (2018).
[65] T. Fukui, Y. Hatsugai, and H. Suzuki, J. Phys. Soc. Jpn. **74**, 1674 (2005).
[66] M. Taherinejad, K. F. Garrity, and D. Vanderbilt, Phys. Rev. B **89**, 115102 (2014).

Figures

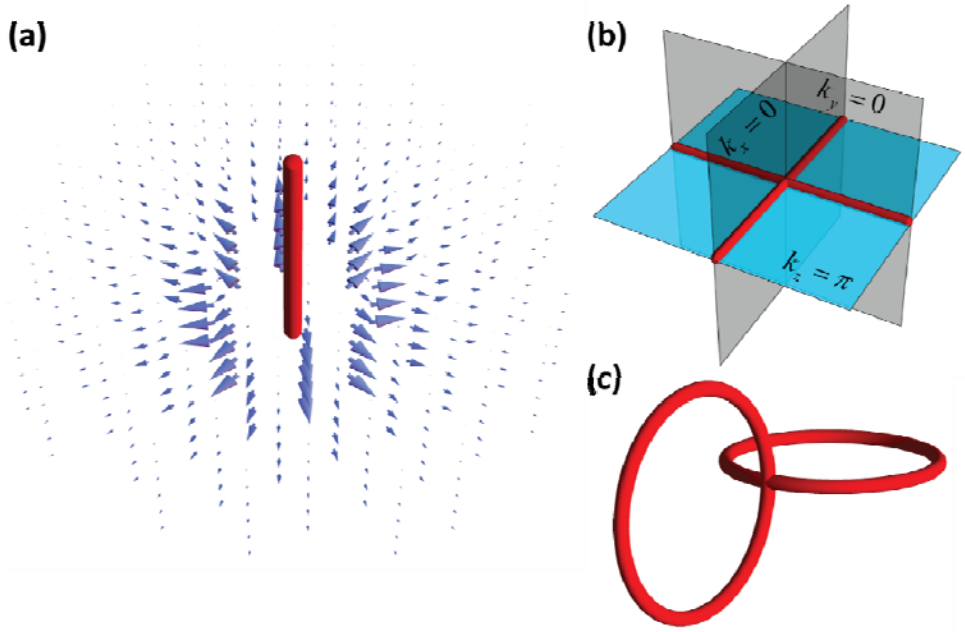

FIG. 1. (a). Berry flux density distribution of a charged nodal line, where the arrows represent the direction and amplitude of the local Berry flux density and the red cylinder represents the charged nodal line. (b). Two nodal lines in the reciprocal space crossing each other can be regarded as two nodal rings chained together (c) as the reciprocal space is periodic.

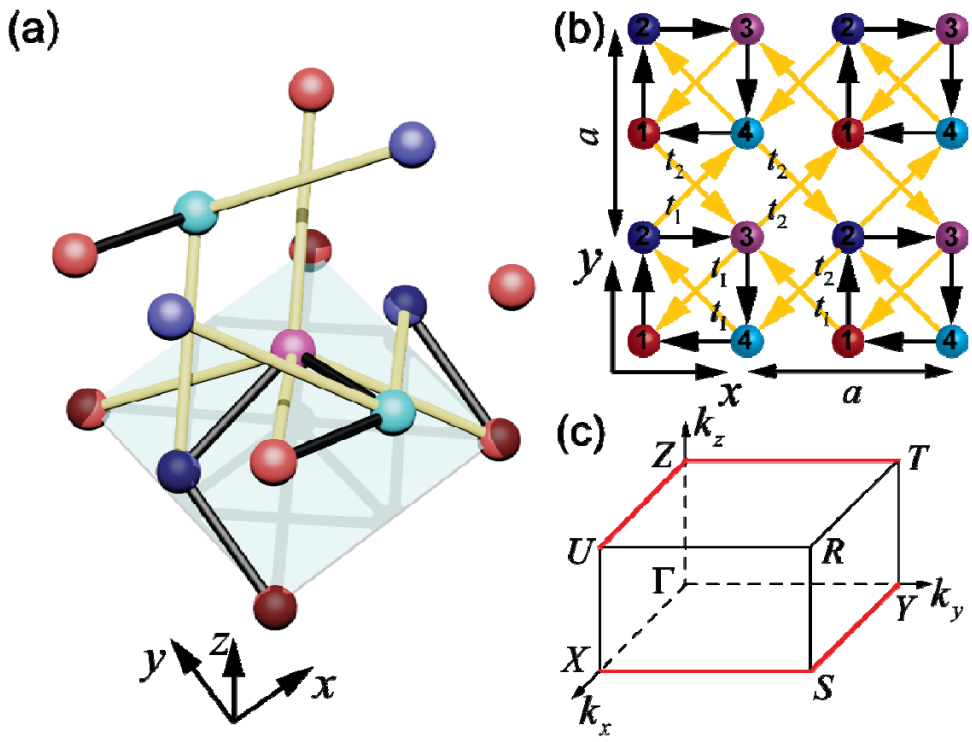

FIG. 2. (a). A sketch of the tight-binding model. The spheres represent lattice sites. Each unit cell consists of four sites with different heights. The heights of the red, blue, magenta and cyan spheres are $h/4$, $2h/4$, $3h/4$ and h, respectively, where h is unit length along the z direction. Black and yellow cylinders represent hopping between nearest neighbor and next nearest neighbor, respectively. The hopping strength represented by the black bonds are the same as denoted by t_0, while that of the yellow bonds are slightly different. The transparent light blue plane is drawn just for better illustration. (b). The projection of the tight-binding model on the xy plane. The projection forms a square lattice with lattice constant a. The number on each sphere represents the height of that sphere. The black and yellow arrows represent respectively, the projection of the black and yellow cylinders in (a), where the arrows point to the upward direction. The hopping strength of the yellow bonds are either t_1 or t_2, as marked in (b). We set $t_1 = (1+\delta)t_c$ and $t_2 = (1-\delta)t_c$, where δ is a small number. (c).The reciprocal space with positions of relevant high symmetric points labeled and nodal lines highlighted in red.

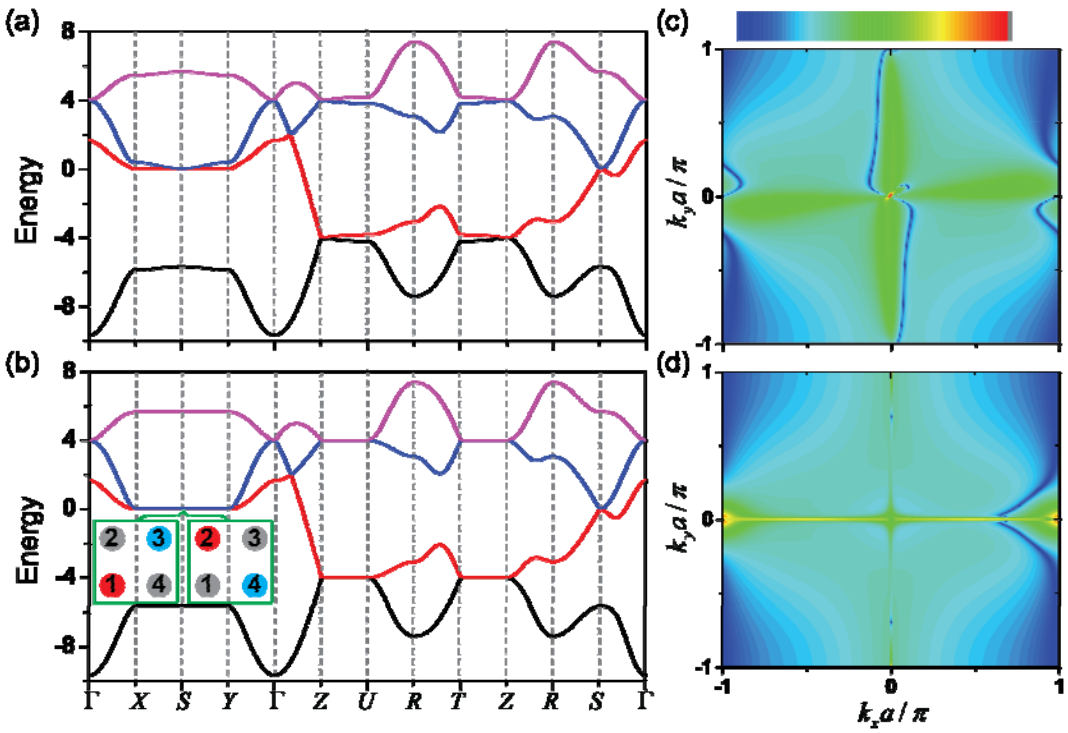

FIG. 3. (a, b).The band structures of the tight-binding model in Fig. 2, where $t_0 = -2\sqrt{2}$, $t_c = -1$, $\delta = 0.1$ for (a) and $\delta = 0$ for (b). The inset in (b) shows the amplitude distributions of the eigenmodes on the flat bands, where red, cyan and gray represent +1, −1 and zero, respectively. Here all the eigenmodes on the flat bands are the same except for a global gauge freedom. The Weyl points at S and Z in (a) get flattened by geometric frustration and form charged nodal lines in (b). The positions of the charged nodal lines are highlighted in Fig. 2(c), which hence form nodal chains in the reciprocal space similar as Fig. 1(c). (c, d). Logarithm of the absolute value of the Berry flux density of the highest band at $k_z h = 0.999\pi$, where (c) and (d) correspond to the band structures in (a) and (b), respectively. Here (c) and (d) share the same color bar, and red (blue) represents maximum (minimum).

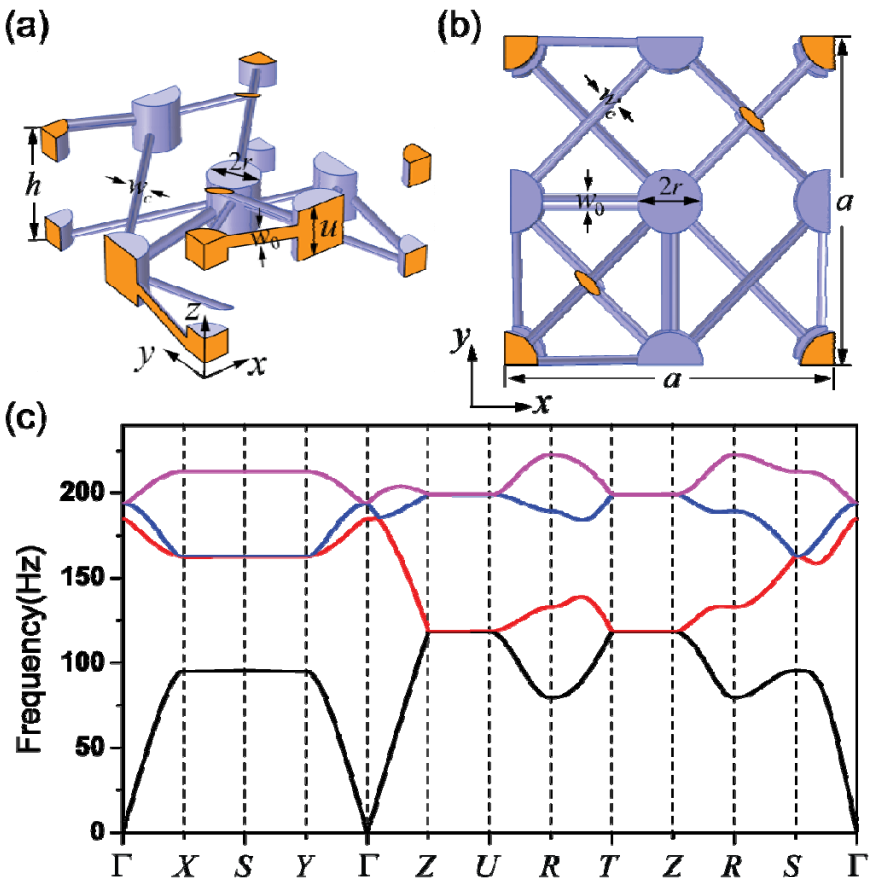

FIG. 4 (a) and (b) show the side view and top view of a unit cell of an acoustic metamaterial which possesses nodal chains with nonzero Berry charges. Here blue and yellow represent the surfaces where hard boundary and periodic boundary conditions are applied, respectively. The system is filled with air (density 1.29kg/m^3 and speed of sound 343m/s). (c) The band dispersion of system along several high symmetry directions, which are quite similar like the tight-binding model. The bands form nodal chain as highlighted in Fig. 2(c). The parameters used are $a = 50\text{cm}$, $r = 5\text{cm}$, $u = 10\text{cm}$, $h = 24\text{cm}$, $w_0 = 2.4\text{cm}$ and $w_c = 1.6\text{cm}$.

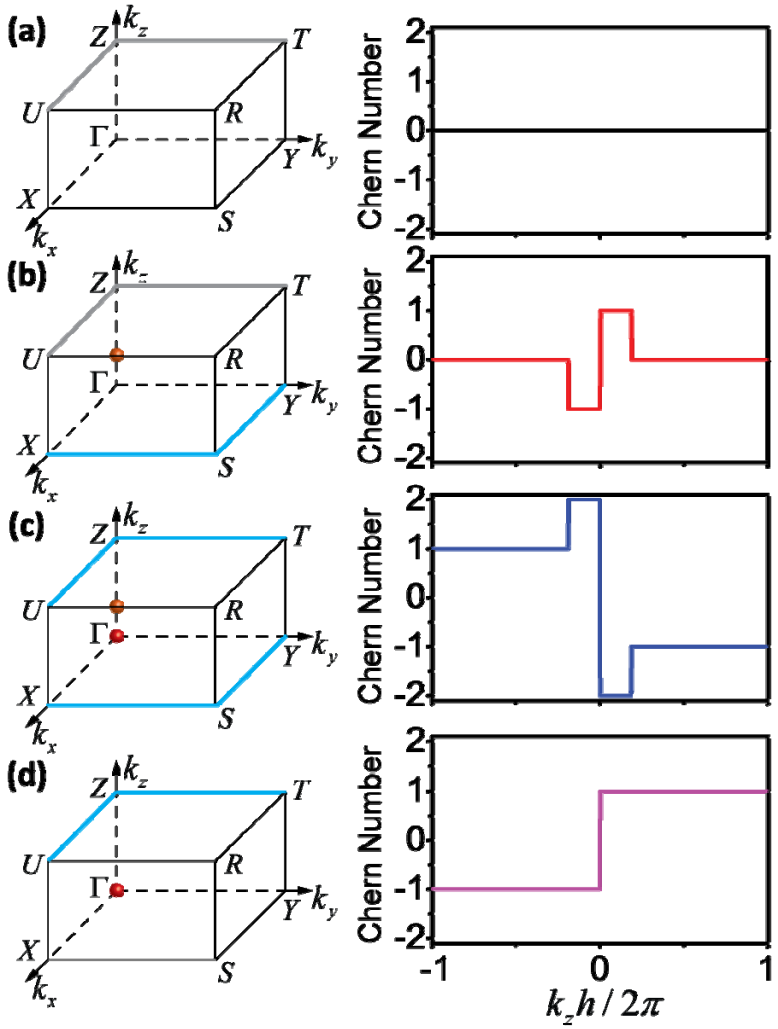

FIG. 5. (a), (b), (c) and (d) show respectively, the charge distributions (left panel) in the reciprocal space and Chern numbers for fixed k_z (right panel) of the first (lowest) band to the forth (highest) band, where the red and orange spheres represent Weyl points with charge +2 and +1, respectively, cyan marks chain degeneracy with Berry charge -2, and gray marks chain degeneracy without Berry charge. The parameters used are the same as Fig. 4.

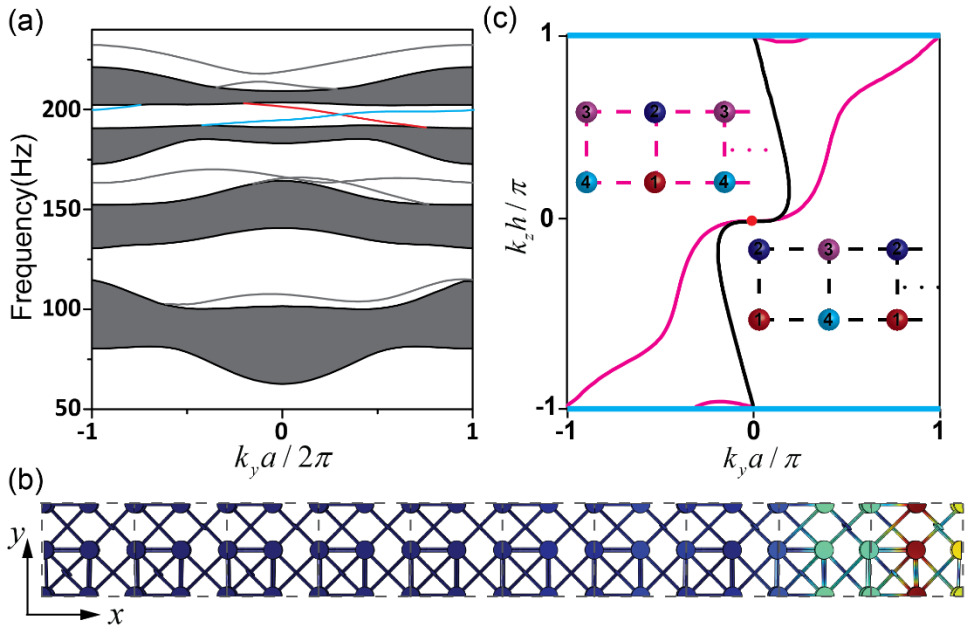

FIG. 6 (a) The gray area represents the projected band structure of a strip of the system (shown in (b)), which is periodic along the *y* and *z* directions, and finite along the *x* direction. The number of unit cell along the *x* direction is chosen to be large enough that the dispersions of the surface states (represented by gray, cyan and red curves) are stable. Here the cyan and red curves represent respectively, one-way edge states localized on the left and right boundary, and gray represents trivial edge state. The color code in (b) represents the absolute value of the eigenpressure distribution of one edge state at $k_y a = 0.1\pi$ and 200.9 Hz, where red and blue correspond to maximum value and zero, respectively. The parameters of the system used are the same as Fig. 4. (c) Fermi-arcs on the $k_y - k_z$ surface Brillouin zone with different truncations calculated with the tight-binding model. We consider a strip of unit cells which is periodic along the *y* and *z* directions, while finite along the *x* direction. Here black and magenta represent the cases when sublattice 1 (2) is the outmost sublattice (the inset on lower right) and sublattice 3 (4) is the outmost sublattice (the inset on the upper left), respectively. The red dot and cyan line represent the projection of the charged +2 Weyl point and the charged -2 nodal chain, respectively. In this calculation, we set $t_0 = -2\sqrt{2}$ and $t_c = -1$ and the energy is fixed at 4, which is also the energy of the nodal lines and Weyl points between band 3 and band 4.

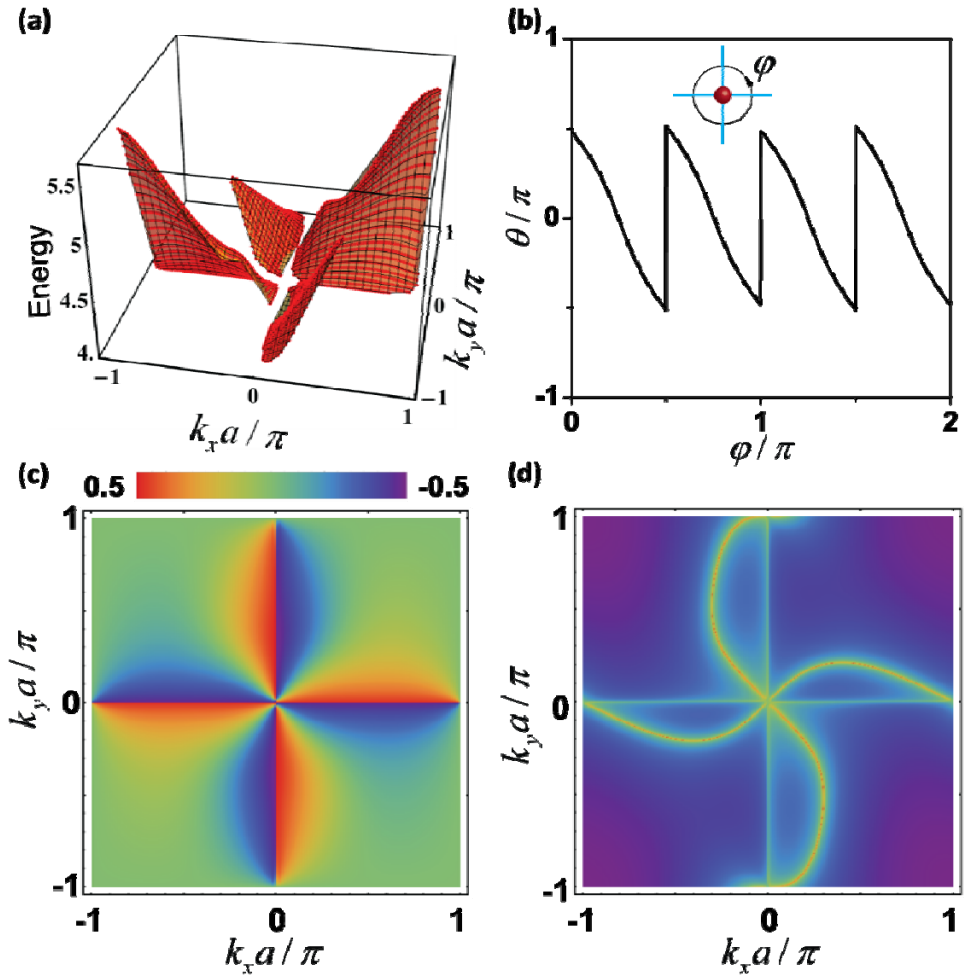

FIG. 7. (a) Spectrum of the surface state between band 3 and band 4 and localized on the upper surface of a strip of the system. The semi-infinite system is semi-finite along the z direction with sublattice 4 on the outmost and periodic along the x and y directions. (b) The Zak phase of band 4 along the black circle as shown in the inset, which is a circle with $a\sqrt{k_x^2+k_y^2}=0.1\pi$ and centers at $k_x=k_y=0$. The cyan lines and red sphere of the inset represent the projection of the nodal chain and the Weyl point, respectively. (c) The Zak phase of band 4 as a function of k_x and k_y. (d) The Fermi-arc at the energy of the nodal chain on the upper surface of a semi-infinite system same as (a) but has sublattice 3 on the outmost. Here we plot the density of state of the unit cell on the surface (surface local density of states). In this calculation, we set $t_0=-2\sqrt{2}$ and $t_c=-1$ and the energy is fixed at 4.

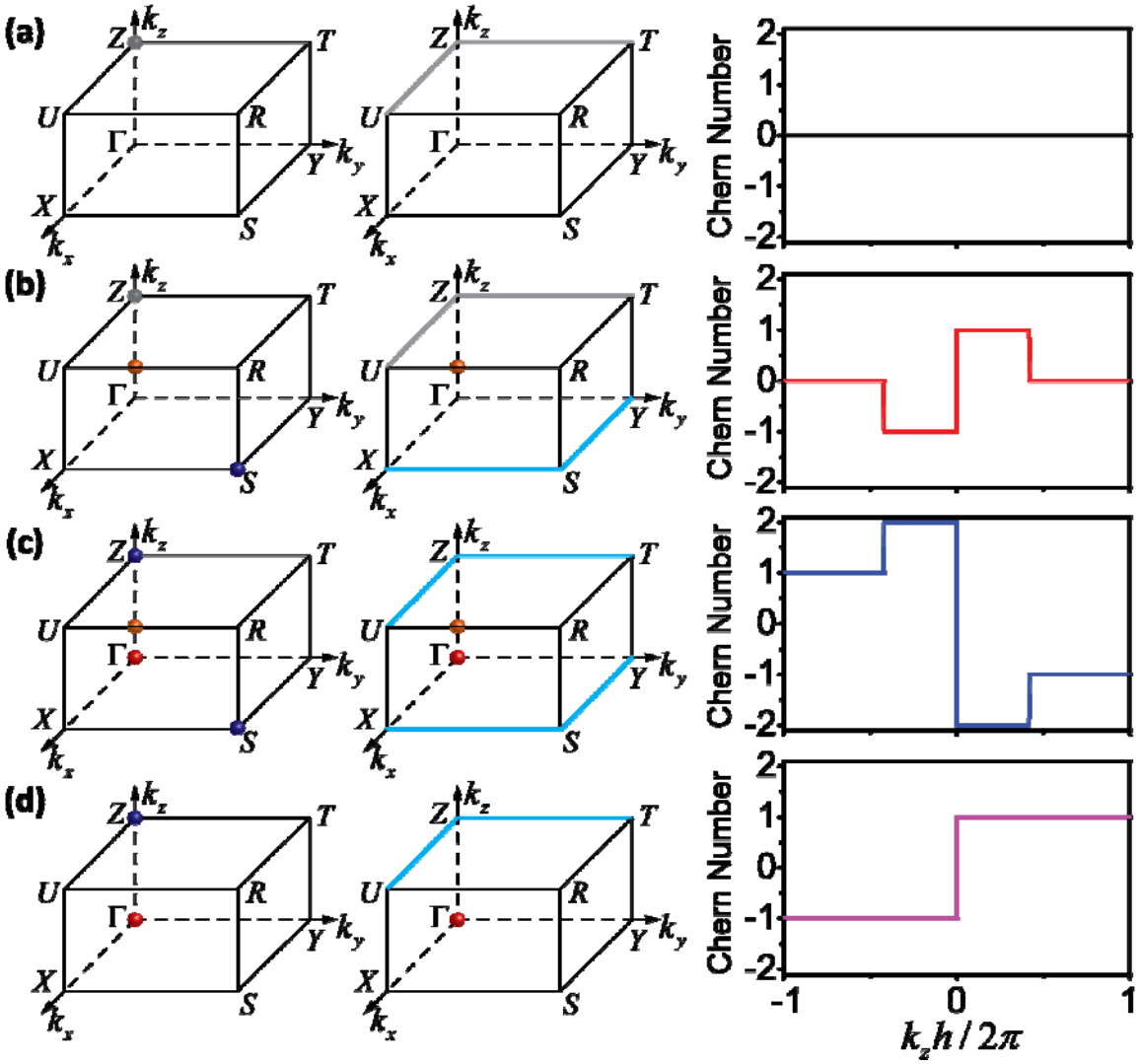

Fig. 8 (a), (b), (c) and (d) show respectively, the charge distributions when $\delta = 0.1$ (left panel) and $\delta = 0$ (middle panel) in the reciprocal space and Chern numbers for fixed k_z (right panel) of band 1 to band 4. Here the Chern number as a function of k_z for left panel and middle panel are the same. On the left and middle panel, the red, orange, and blue spheres represent Weyl points with Berry charges +2, +1 and -2, respectively, the cyan lines denote line degeneracy with charge -2, and the gray sphere and lines denote point and line degeneracy without Berry charge. Here the tight binding model in Eq. (A1) with $t_0 = -2\sqrt{2}$ and $t_c = -1$ is assumed.

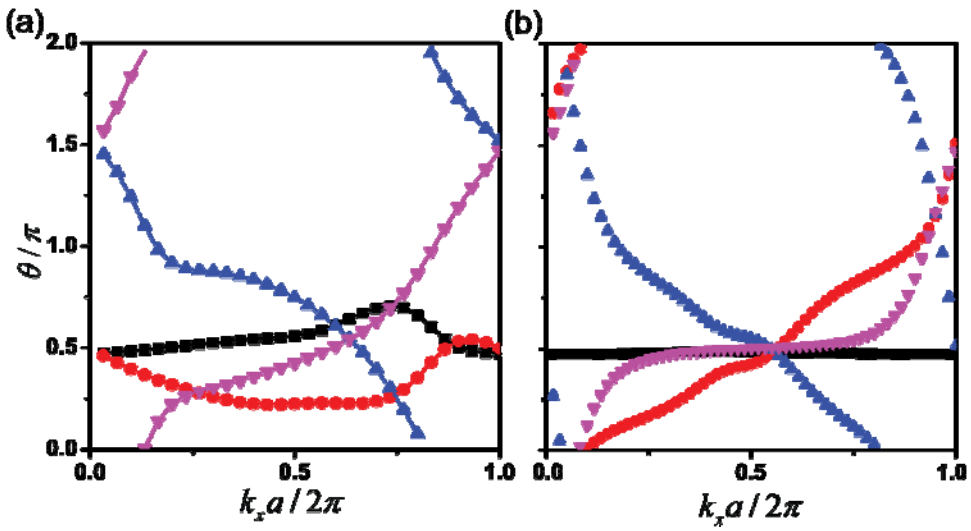

Fig. 9 The Zak phase of each band as a function of k_x for fixed $k_z h = 0.5\pi$ (a) and $k_z h = 0.1\pi$ (b), where black, red, blue and magenta represent the Zak phases of band 1, 2, 3 and 4, respectively. The geometric parameters of system under consideration are the same as Fig. 4.